Reevaluation of metal interconnectivity in a partially molten silicate matrix using 3D microtomography

Adrien Néri, Jeremy Guignard, Marc Monnereau, Misha Bystricky, Jean-Philippe Perrillat, Denis Andrault, Andrew King, Nicolas Guignot, Christophe Tenailleau, Benjamin Duployer, et al.

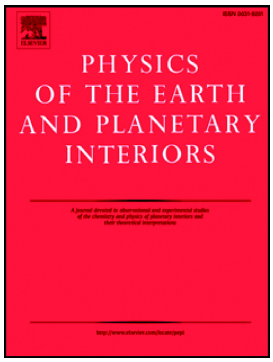

Reevaluation of metal interconnectivity in a partially molten silicate matrix using 3D microtomography

Adrien Néri, Jérémy Guignard, Marc Monnereau, Misha Bystricky, Jean-Philippe Perrillat, Denis Andrault, Andrew King, Nicolas Guignot, Christophe Tenailleau, Benjamin Duployer, Michael J. Toplis, Ghylaine Quitté

PII: S0031-9201(20)30119-9

DOI: https://doi.org/10.1016/j.pepi.2020.106571

Reference: PEPI 106571

To appear in: *Physics of the Earth and Planetary Interiors*

Received date: 23 April 2020

Revised date: 3 August 2020

Accepted date: 21 August 2020

Please cite this article as: A. Néri, J. Guignard, M. Monnereau, et al., Reevaluation of metal interconnectivity in a partially molten silicate matrix using 3D microtomography, *Physics of the Earth and Planetary Interiors* (2020), https://doi.org/10.1016/j.pepi.2020.106571

Reevaluation of metal interconnectivity in a partially molten silicate matrix using 3D microtomography

Adrien Néri[a,*], Jérémy Guignard[a,&], Marc Monnereau[a], Misha Bystricky[a], Jean-Philippe Perrillat[b], Denis Andrault[c], Andrew King[d], Nicolas Guignot[d], Christophe Tenailleau[e], Benjamin Duployer[e], Michael J. Toplis[a], Ghylaine Quitté[a]

[a]IRAP, Université de Toulouse, CNRS, CNES, UPS, Toulouse, France

[b]Université de Lyon, Université Lyon 1, ENS de Lyon, CNRS, UMR 5276 Lab. de Géologie de Lyon, Villeurbanne F-69622, France

[c]Université Clermont Auvergne, CNRS, IRD, OPGC, Laboratoire Magmas et Volcans, F-63000 Clermont-Ferrand, France

[d]Synchrotron SOLEIL, L'Orme des Merisiers, Saint-Aubin, BP 48, 91192 Gif-sur-Yvette, France

[e]CIRIMAT, CNRS-INP-UPS, Universite de Toulouse, 118 route de Narbonne, 31062 Toulouse Cedex 9, France

[&]Now at CNRS, UMR 6112, Université de Nantes, Laboratoire de Planétologie et Géodynamique, Nantes, France

[*]Corresponding author, Present address: Bayerisches Geoinstitut, University of Bayreuth, 30 Universität Str., 95447 Bayreuth, Germany

e-mail address: adrien.neri@uni-bayreuth.de

Keywords: metal-silicate differentiation, 3D microtomography, interconnectivity, textural maturation, planetesimals, primitive achondrites

Abstract

Understanding metal-silicate differentiation in small rocky bodies that accreted early in solar system history requires quantification of the effects of variable amounts of silicate melt and molten metal on the connectivity of metal-rich liquids. To shed light on this question, the equilibrium geometry and textural ripening of metal grains in the vicinity of the metal interconnection threshold have been determined experimentally. High pressure and temperature experiments were performed in the three-phase system forsterite + silicate melt + nickel at conditions of 1 GPa and from 1773 K to 2080 K using piston-cylinder and Paris-Edinburgh presses. Sample microstructures were analyzed by 3D X-Ray microtomography either *in-situ* at the PSICHE beamline of the SOLEIL synchrotron, or on quenched samples using a laboratory Computed Tomography scan. Although dihedral angles point to textural equilibrium at the scale of individual grains at the end of each experiment, the attainment of textural equilibrium at sample scale is not straightforward. Depending on the relative proportions of the phases, different degrees of textural maturation are revealed. A particularly important issue is that time-resolved *in-situ* microtomography data show that cold (subsolidus) compression at the beginning of the experiment leads to soft metal grains being squeezed between silicates, leading to a forced interconnectivity of nickel. High temperature experiments with metal contents ≤ 20 vol% resulted in disruption of these forced networks, while the networks persisted in time for metal contents ≥ 25 vol%. This is taken to indicate that the stable interconnection threshold of pure nickel in a partially molten silicate matrix lies between 20 and 25 vol%. Therefore, we conclude that care must be taken when defining the interconnection threshold: not only should there be existence of a network of touching grains, but this network must persist in time in the absence of external forces and at pressure-temperature conditions that permit grain-boundary movement (i.e. excluding kinetically arrested systems).

Growth of silicate grains is identified as the process driving textural maturation, and may explain the variability of interconnection thresholds reported in the literature. In addition, these considerations shed light on the diversity of textures observed in natural meteoritic samples (e.g. carbonaceous and ordinary chondrites and primitive achondrites), providing textural arguments to constrain the processes that affected these meteorites.

1. Introduction

Terrestrial planets and their natural satellites (e.g. the Earth's Moon (Righter, 2002) and even icy moons such as Ganymede (Anderson et al., 1996; Kivelson et al., 1996; Schubert et al., 1996)) show evidence for metallic cores, as inferred from their magnetic fields, reduced momentums of inertia or geochemical composition. However global-scale evolution processes have affected these bodies, wiping out direct evidence of differentiation conditions and mechanisms. The meteorite record on the other hand constitutes an alternative and a better-preserved window into differentiation processes in the early solar system. Meteorites cover a large variety of objects that can be classified into three main categories depending on their degree of differentiation: chondrites (undifferentiated), achondrites (fully differentiated) and primitive achondrites (partially differentiated, achondritic textures). Based upon study of these objects, two different scenarios of metal-silicate differentiation have been proposed:

(1) Study of achondrites has led to the scenario of large-scale melting processes of their parent bodies. This idea is supported by the formation of iron meteorites that requires complete melting of the iron-sulfur subsystem (Chabot and Haack, 2006; Goldstein et al., 2009 and references therein), implying the presence of a large fraction of silicate melt. Additionally, the homogeneous oxygen isotopic composition of the HED clan (i.e. Howardite - Eucrite - Diogenite) argues in favor of a global magma ocean (Greenwood et al., 2014). In this scenario, metal segregation may have occurred by particle settling.

(2) The study of primitive achondrites on the other hand leads to the idea of incomplete metal-silicate segregation at low degrees of partial melting. Among the subgroups of this clan, acapulcoites and lodranites are of particular interest, as they have not generally been subject to shock, oxidation or large-scale alteration (Keil and McCoy, 2018). Acapulcoites exhibit the lowest degree of differentiation and are thought to have been heated just above the onset of melting of silicate and iron-sulfide subsystems, i.e. at T ≈ 1270 K (e.g. McCoy et al., 1996; Mittlefehldt et al., 1996). Some objects experienced extraction of silicate (< 5 vol%) and iron-sulfide melts, as evidenced by depletion in incompatible elements (Mittlefehldt et al., 1996; Palme et al., 1981; Patzer et al., 2004; Zipfel et al., 1995). In contrast, lodranites represent a more evolved subgroup with complete loss of early melting silicates such as feldspars and clinopyroxenes and a metallic subsystem strongly depleted in sulfur. Such features point to the extraction of both silicate and iron-sulfide melts (Bild and Wasson, 1976; McCoy et al., 1997) at temperatures of ≈ 1473 K, consistent with a degree of silicate melting of 20-25 vol% (Bild and Wasson, 1976; McCoy et al., 1997, 1996; Papike et al., 1995). In this scenario, metal-sulfide may have been extracted by percolation, forming a connected network through a polycrystalline silicate matrix.

The dynamics of interconnection and disruption of metallic networks are thus of prime importance when considering metal-silicate differentiation in rocky bodies of the solar system. The interconnection of the metallic phase requires volume fraction to be above a critical interconnection threshold, i.e. the phase fraction at which a 3D network is generated. In theory, this threshold can be considered as the result of the minimization of interfacial energies between the different phases (Bulau et al., 1979; Jurewicz and Watson, 1985; Smith, 1964). This

energetic balance favors low-energy contacts at the expense of high energy ones and is expressed physically by the dihedral angles at triple junctions. In a two-phase system, the dihedral angle θ of the liquid between two solid grains is a function of the interfacial energy between them $\gamma_{Solid\text{-}Solid}$ and that between the solid and the liquid $\gamma_{Solid\text{-}Liquid}$ (in $J.m^{-2}$), following (Smith, 1964):

$$2\cos\frac{\theta}{2} = \frac{\gamma_{Solid-Solid}}{\gamma_{Solid-Liquid}} \quad (1)$$

From a theoretical point of view, for $\theta < 60°$, the interconnection threshold is vanishingly small (i.e. the phase is interconnected at all melt fraction: see Laporte and Provost (2000) and references therein), while for $\theta > 60°$, an increasing amount of the phase of interest is required to form an interconnected network.

Dihedral angles reported for mafic and ultramafic silicate melts in an olivine matrix are lower than 60° (Faul, 2000; Laporte and Provost, 2000); the formation of an interconnected network for this phase is thus easily achieved. On the contrary, metallic melts have dihedral angles greater than 60°, with values varying as a function of sulfur and oxygen content (Holzheid et al., 2000; Néri et al., 2019; Rose and Brenan, 2001). The dependence of the interconnection threshold on sulfur content has consequences for the low pressure (<1 GPa) segregation of iron-sulfide melts, as the composition of the latter varies as a function of temperature. The first melt produced along the Fe-S join at these pressure conditions is sulfur-rich (eutectic composition) and has a relatively low dihedral angle (Ballhaus and Ellis, 1996; Gaetani and Grove, 1999; Holzheid et al., 2000; Minarik et al., 1996), with values ranging from 60° to 100°, i.e. interconnection thresholds from 0 to 7 vol% (estimated from Wray, 1976). Segregation is thus promoted in iron-sulfur alloys relative to the other end-member, pure metal. The latter displays much larger dihedral angles (Gaetani and Grove, 1999; Néri et al., 2019; Shannon and Agee, 1996) from 110° up to 176° corresponding to theoretical interconnection thresholds ranging from 10 to 25 vol%.

Discrepancies exist between dihedral angles inferred in different studies for similar compositions of metallic melts, a situation which is most likely due to the different resolutions used to assess dihedral angles on SEM images (Cmíral et al., 1998; Néri et al., 2019). Electrical conductivity measurements can also be used to determine the interconnection threshold, but literature data also show large variations in the values obtained for the same composition. For instance, a low threshold of 3 to 6 vol% has been estimated by Watson and Roberts (2011) and Yoshino et al. (2003) for the Fe-FeS eutectic composition, while Bagdassarov et al. (2009) reported a much higher value of 17.5 vol%. This discrepancy is possibly explained by different degrees of textural maturation (Bagdassarov et al., 2009) driven by grain boundary migration (Bagdassarov et al., 2009; Walte et al., 2007).

All the techniques used to assess the interconnection threshold discussed above are based on the 1D or 2D properties of the samples (electrical conductivity, dihedral angles) and more data are clearly required to reconcile the microstructural observations (dihedral angles) with bulk (e.g. electrical conductivity) and macroscopic properties. Indeed, similar microscopic equilibrium properties can lead to different macroscopic textures (Néri et al., 2019). The present study aims to bring new constraints on this problem by studying the effect of varying silicate and metallic melt contents on the 3D distribution of the metallic phase in a system composed of forsterite, silicate melt and pure metal. 2D-microstructures of this system have already been investigated (Néri et al., 2019) and show no variations of dihedral angles as a function of the relative proportions of the different phases or the run duration. Hence the present study focuses on the meso- to macro-scale distribution of metal.

To constrain the influence of varying the amount of silicate and metallic melts, experiments were conducted at high pressure to remove porosity, or at least prevent remaining porosity from expanding due to thermal dilation and to ensure that the equilibrium geometries of large metallic grains are not affected by the motion of gas bubbles. Experiments were performed at 1 GPa using a piston-cylinder (PC) and a Paris-Edinburgh (PE) press. This pressure is larger than that expected at the center of a rocky body even the size of Vesta (≈ 300 km in radius). However, it enabled well controlled experiments that are of relevance given that pressure has little effect on phase equilibria (e.g. Presnall et al. (1978) and Buono and Walker (2011) for silicate and Fe-S systems respectively) and interfacial energies (see Section 3.1) in the range 1 bar to 1 GPa.

The characterization of the 3D distribution of the metal was performed using *ex-situ* 3D X-Ray microtomography on recovered samples (piston-cylinder experiments), as well as *in-situ* microtomography at the PSICHE beamline (Paris-Edinburgh press experiments at the SOLEIL synchrotron) to obtain time-resolved information on textural evolution in the presence of silicate melt. Results reveal that the initial compression of the experiment forces macro-scale textures that are far from the equilibrium indicated by micro-scale dihedral angles (see below). The subsequent textural maturation and the approach to textural equilibrium are then highly dependent on grain growth processes.

2. Experimental setup

2.1 Starting material

Samples were mixtures of crystalline forsterite (Fo), synthetic silicate melt (Melt) and nickel metal (Ni) with different modal abundances. Two compositions of silicate melt in the Anorthite-Diopside-Forsterite (An-Di-Fo) system were synthesized (Table 1). The first one represents a composition in equilibrium with forsterite at 1773 K and 1 GPa (Presnall et al., 1978) and was used in PC experiments. In this way, the relative proportions of forsterite and silicate melt can be varied without changing their composition. The second melt has the composition of the An-Di-Fo eutectic (1653 K) at 1 GPa (Presnall et al., 1978). This composition was used for PE experiments to allow progressive melting of the silicates during heating. Each silicate melt was synthesized in the form of a glass following the procedure described in Néri et al. (2019). Their composition was controlled by Electron MicroProbe analyses (EMPA) at the Raimond Castaing Center (Toulouse, France). At least 30 measurements were made randomly on the surface of a piece of each glass; compositions matched that given in Table 1 within 1 wt%. Recovered glasses were then finely ground and mixed with Fo and Ni in the desired proportions (see Table 2). In the remainder of the text, sample mixtures are expressed as <Fo : Melt : Ni> in vol%.

Although iron is the most abundant metal in natural samples, nickel was used in the present experiments as its lower melting temperature and its stability at higher oxygen fugacity (fO_2) allow a better control of the chemistry and mineralogy of the samples. Besides, previous work with similar experimental systems (Néri et al., 2019) showed that the diffusion of nickel into the silicate phases is very limited under experimental conditions (≈ 2 wt% NiO in forsterite and ≈ 0.6 wt% NiO in silicate glass at equilibrium).

2.2 Experiments

2.2.1 Piston-cylinder experiments (PC)

Piston-Cylinder (PC) experiments were performed in a ¾-inch solid medium apparatus at the Laboratoire Magmas et Volcans (LMV, Clermont-Ferrand, France) for 4 hours at 1 GPa and 1773 K, i.e., 20 K above the

melting point of nickel at this pressure (Strong and Bundy, 1959). Temperature was measured using a type C thermocouple (WRe_5 / WRe_{26}) and controlled using a PID Eurotherm controller. The uncertainty on temperature was ±5 K. Powder mixtures were directly loaded in a graphite capsule, making the sample size about 3 mm^3. Graphite was chosen to buffer the oxygen fugacity and to limit interaction with silicates. Although carbon is expected to dissolve into molten nickel, this effect was limited during the duration of the experiment and no graphite crystals were found as inclusions in the quenched nickel beads. The graphite capsule was then put into a MgO sleeve to isolate it from the graphite furnace and MgO spacers were used to align the sample with the hot zone. To limit shear and to mechanically stabilize the assembly, pyrex tubes were added on both sides of the graphite furnace. This assembly was contained in a NaCl cell to ensure hydrostatic conditions (Figure 1a).

2.2.2 Paris-Edinburgh press experiments (PE)

Paris-Edinburgh (PE) press experiments were used to acquire time-resolved information using *in-situ* 3D X-Ray microtomography (beamline PSICHE, SOLEIL Synchrotron). In this case, forsterite powders were sieved to grain sizes larger than 30 µm, allowing better imaging of individual grains. The Ultrafast Tomography Paris-Edinburgh Cell (UToPEC) was used (Boulard et al., 2020, 2018). This equipment allows the acquisition of a full image of the sample in a few tens of seconds, and also offers a 165° angular opening (upon a 180° rotation) that reduces artifacts during reconstruction (Boulard et al., 2020, 2018). Samples were first taken to a pressure of 1 GPa, then temperature was progressively increased. A pink beam (filtered white beam with an average energy of 63 keV) was used to produce the high photon flux necessary for high temporal, i.e. < 1 min per tomogram, and spatial, i.e. 1.3 µm voxel size, resolutions. Pressure and temperature were determined using the cross calibration method (Crichton and Mezouar, 2002) using the diffraction lines of Pt and hBN powders and equations of state from Le Godec et al. (2000) and Zha et al. (2008). The P-T calibrants were placed near the furnace but not in direct contact with the sample. Temperature uncertainties with this method are estimated to be ±50 K.

As for PC experiments, powder mixtures were loaded in an inner graphite capsule, and a hBN outer capsule. Samples were 2.1 mm in height and 1.2 mm in diameter. Graphite and molybdenum disks and steel rings were placed on both vertical ends of the furnace to align the sample vertically and to ensure electrical conductivity. This assembly was contained in a boron epoxy pressure medium to ensure hydrostatic conditions (Figure 1b). A PEEK plastic ring was added around the boron epoxy cell to limit extrusion of the assembly.

For these experiments, the starting silicate melt content corresponds to the eutectic silicate melt content. For instance, for the <65 : 25 : 10> mixture, 25 vol% of silicate melt is expected just above the eutectic temperature. Increasing the temperature during the experiment thus leads to progressive melting. The melt content can thus be calculated at each temperature step from the Anorthite-Diopside-Forsterite ternary diagram at 1 GPa (Presnall et al., 1978) using the lever rule.

2.3 Analytical techniques

2.3.1 Ex-situ 3D X-Ray microtomography

The spatial distribution of the metal in quenched PC samples was characterized with non-destructive 3D X-ray Computed Tomography (CT), using a Phoenix/GE Nanotom 180 from the French FERMAT federation (Toulouse, France). Operating conditions were 100 kV voltage and 130 µA current. For a complete CT-scan, 1440 slices were measured with an angular resolution of 0.25° and a 1.5-1.8 µm voxel size. Each slice corresponds to the acquisition of 5 images (750 ms per image); the first one was discarded to avoid remanence effects on the

detector while the other four are stacked to increase the signal to noise ratio. Typical acquisition time was 1.5 hours per CT-scan. Data were processed with Datosx reconstruction software to obtain the 3D reconstructed volumes.

Our 3D X-Ray microtomography set-up allows the detection of nickel grains (or assemblage of grains) that have a volume larger than 6 voxels. The physical size of the detection limit thus depends on the resolution of the acquisition. In the present case, the voxel size varies between 1.5 and 1.8 µm, fixing the lower detection threshold to grains that have a sphere-equivalent diameter greater than 3.4 to 4.1 µm. The proportion of Ni grains that are below this detection threshold represents less than 1 % of the initial grain size distribution.

2.3.2 In-situ 3D X-Ray microtomography

In-situ data collected using the ultra-fast microtomography set up available on beamline PSICHE at SOLEIL allows conducting time-resolved analyses of the textural evolution of a sample at the scale of an experiment. Indeed, the high photon flux of synchrotron radiation enables the acquisition of a complete CT-scan in 50 s. 1500 slices were acquired for each scan with an angular resolution of 0.24° and a 1.3 µm voxel size. Each slice consists of a single image with an exposure time of 35 ms. Raw data were processed with a Paganin filter to enhance phase contrasts (Paganin et al., 2002) and the backprojection PyHST2 algorithm (Mirone et al., 2014) was used to reconstruct the 3D volumes.

To allow the best possible comparison between different microtomograms acquired at different temperatures for the same experiment, quantitative data were extracted from the same region of interest within the sample.

2.3.3 3D data processing

The 3D volumes were first converted into a stack of 8-bit images using ImageJ (Eliceiri et al., 2012; Schindelin et al., 2012) and representative Regions of Interest (RoIs) with dimensions of 500 x 500 x 500 voxels (i.e. volumes of 0.3 to 0.7 mm^3) were extracted. These stacks were then loaded into Blob3D (Ketcham, 2005) for quantitative data analysis in three steps: segmentation, separation and extraction. For the "segmentation", the software identifies a given set of voxels with particular grayscale values and assigns them to a given phase. In the present case, the grayscale difference between forsterite and silicate melt could not be resolved due to similar X-ray absorption coefficients and densities. Hence, only two phases were segmented: nickel and "silicates", the latter including forsterite and silicate melt. Segmentation involved a simple thresholding, i.e. nickel is selected as the population of voxels above a threshold grayscale value that is adjusted such that the total volume of nickel corresponds to the initial content within the sample. No additional filters (e.g. smoothing, erode, dilate, etc…) were applied. In the "separation" step, the different sets of contiguous voxels are distinguished in terms of distinct objects, or blobs (see Ketcham (2005) for more details). Finally, "extraction" provides a quantitative analysis of the separated objects: their volume, surface, Normalized Surface (NS, i.e. the surface of the blob normalized to that of a sphere of the same volume, a parameter that quantifies deviations from spherical shape), their orientation and maximum and minimum lengths. Of these parameters, only volume, surface and NS were used in our microstructural analysis as they are the most useful in representing the complex shape of nickel grains observed in our experiments. Extracting these parameters from representative RoIs is an efficient way to acquire statistical information on the large-scale geometry of nickel grains and to determine textural trends between the different experiments (e.g. NS, number of grains, mean volume). To investigate errors induced by the thresholding method, the threshold was varied by one graylevel above and below its reference value. This exercise result-

ed in a change of the absolute Ni content of less than 1 vol% for most experiments and did not significantly affect the extracted textural parameters (see Figure S1).

2.3.4 SEM imaging

The small-scale geometry of nickel grains and dihedral angles at triple junctions were also quantified by Field Emission Gun Scanning Electron Microscopy (FEG-SEM). Post-experiment samples were mounted in epoxy resin and finely polished down to 1/30 µm with colloidal silica. The FEG-SEM images were acquired at the Raimond Castaing Center (Toulouse, France) using a JEOL JSM-7800F Prime FEG-SEM, operated with a 10 keV accelerating voltage and 10 nA beam current.

Repeated dihedral angle measurements on at least 300 triple junctions were conducted on high resolution images (30 nm pixel size) using ImageJ. Errors on dihedral angles were estimated from two Standard Errors (SE), i.e. $2\ \frac{SD}{\sqrt{N}}$ with SD the standard deviation and N the number of measurements. For more details on dihedral angle measurements and data processing, the reader is referred to Néri et al. (2019).

3. Results

A total of 10 experiments were performed. Experimental run conditions, relative proportions of each phase, pressure and temperature, are provided in Table 2.

3.1 Attainment of textural equilibrium at the grain scale

FEG-SEM images were used to assess micro-textural equilibrium. These images show olivine triple junctions at 120° in all samples. Typical sample micro-textures are shown in Figure 2 for the <76.5 : 8.5 : 15> (Figure 2a) and <72 : 8 : 20> (Figure 2b) mixtures (expressed in <Fo : Melt : Ni> vol%). Textures indicate that nickel does not wet olivine grain boundaries, while silicate melt seems to form thin wedges close to triple junctions. Such features are confirmed by dihedral angle measurements, which yield values of 25, 150 and 175° for silicate melt, forsterite and nickel respectively. These results are very similar within uncertainties to those of Néri et al. (2019) and indicate that the interfacial energies (γ) of this system can be ordered as follows: $\gamma_{\text{Melt-Olivine}} < \gamma_{\text{Melt-Nickel}} < \gamma_{\text{Nickel-Olivine}}$ ("Melt" refers here to the silicate melt). This relative order of interfacial energies highlights the fact that silicate melt is the phase with the greatest tendency to wet other grains, and nickel the phase with the least tendency to wet other grains. On the other hand, while the interfacial energy between olivine and nickel is the highest, there is always contact between these two phases. This is because the condition for nickel to be completely surrounded by silicate melt (i.e. without any contact with forsterite grains) is: $\gamma_{\text{Melt-Nickel}} > (\gamma_{\text{Melt-Olivine}} + \gamma_{\text{Nickel-Olivine}})$, a condition that is not satisfied here (see Néri et al., 2019).

The observations described here thus indicate that micro-textural equilibrium was reached during the duration of the experiments (i.e. a few hours), at least at the grain scale. Taken at face value, the extremely high dihedral angle of Ni implies a high interconnection threshold for pure metal compositions, on the order of 25 vol% using the formula proposed by Wray (1976) for two-phase systems. On the other hand, as shown in Section 3.2, the macro-scale organization of metal grains is different from one experiment to another, depending on the relative proportions of the different components. We stress that similar micro-textural equilibria can lead to different macroscopic textures as illustrated and discussed below.

3.2 Effect of varying silicate melt content and metal fraction

Starting mixtures are composed of phases with highly different rheological properties: a soft metal in a matrix of rigid silicates. As detailed in Section 3.2.2, these different rheologies lead to an initial state, just after compression, of textures that are far from the equilibrium expected from grain-scale minimization of interfacial energies. The *ex-situ* analyses presented in 3.2.1 thus provide insights into the effect of varying silicate melt and metal fraction on the textural maturation of the systems, while *in-situ* analyses presented in Section 3.2.2 highlight the evolution of textures, from the initial post-compression state to a texturally mature state.

3.2.1 Ex-situ analyses

A series of experiments with molten nickel was performed to study the effect of varying silicate melt and metal contents on the equilibrium texture and the formation of an interconnected network. PC experiments were run with 10, 15 and 20 vol% of nickel and three different forsterite to forsterite plus silicate melt ratios (noted as Fo/(Fo+Melt)): 90, 80 and 70%. These experiments were kept at 1773 K and 1 GPa for 4 hours (Table 2).

Figure 3 shows the five largest metal blobs among the thousands detected on CT-scan images, and illustrates the changes in nickel morphologies with varying phase proportions. For a high Fo/(Fo+Melt) fraction of 90% and a low nickel fraction of 10 vol% (Figure 3a), nickel blobs have rounded shapes, forming either isolated spheres or spheres in contact through narrow necks. However, increasing the nickel volume fraction to 20 vol% allows the formation of small and localized networks with irregular shapes that largely deviate from spherical shape (Figure 3c). The sample with 15 vol% of nickel shows an intermediate situation, with the largest blobs having shapes that are either close to an aggregate of spheres (e.g. the red or green blobs on Figure 3d) or that are highly irregular (e.g. the red blob on Figure 3b). Increasing the silicate melt fraction (decreasing Fo/(Fo+Melt)) precludes the formation of these small localized networks observed in <76.5 : 8.5 : 15> and <72 : 8 : 20> mixtures (Figure 3b and 3c). Instead, blobs have shapes that are close to an aggregate of spheres or to spheres (Figure 3d-g). At these lower Fo/(Fo+Melt) ratios, varying nickel content does not seem to affect the shape of the blobs but only their size.

From the extracted volume and surface data, two types of representation are presented. (1) *Normalized Surface (NS) as a function of blob volume*. This value corresponds to the surface of the blob normalized to that of a sphere of the same volume and accounts for the irregular shape of blobs compared to a spherical shape. The NS of detected blobs can be compared to that of simple geometric shapes (e.g. elongated cylinders), illustrating how blobs deviate from such reference shapes. In this work, NS values of the blobs in our experiments are compared with a cylinder of different aspect ratios, defined by the height to diameter ratio (e.g. Figure 4 first row). (2) *Grain size distribution in terms of volume fraction*. In this case, the volume fraction of nickel of each bin is normalized to the total nickel content of the sample (e.g. Figure 4 second row).

Figure 4 represents the quantitative data for all detected blobs. As also observed qualitatively in Figure 3, at a high Fo/(Fo+Melt) fraction of 90% (Figure 4a-c red dots) and at a low nickel fraction of 10 vol% (Figure 4a), blobs have cylinder equivalent aspect ratios (height to diameter) that do not typically exceed 10, meaning that they are close to spherical but are mostly formed of an aggregate of spheres, generating the observed geometric characteristics. Increasing the nickel fraction to 15 vol% does not significantly change the NS populations within the sample (Figure 4b). However, the experiment with 20 vol% nickel (Figure 4c) shows blobs that have a cylinder equivalent aspect ratio up to 100, thus deviating largely from a sphere. This feature occurs only for large blobs ($\geq 10^5$ µm^3); smaller blobs do not show such irregular shapes and seem closer to spherical, which may be a resolution effect. Finally, at a given metal fraction, varying Fo/(Fo+Melt) ratios gives different NS distributions:

blobs have lower cylinder equivalent aspect ratios with decreasing Fo/(Fo+Melt) ratio, describing the fact that their shapes are closer to spheres (Figure 4b and 4c, blue and green dots).

Grain size distributions of the different samples provide additional information. For a nickel content of 15 vol% (Figure 4d and 4e), the volume fraction distributions are very similar irrespective of the Fo/(Fo+Melt) ratio. Variations in the minimum grain size detected depend on the resolution of the microtomography acquisition, but are not significant. These distributions are characterized by a maximum blob size that does not exceed ≈ 3.10^5 µm^3 and the largest blob represents up to 1% of the total nickel of the sample. For larger nickel contents of 20 vol% (Figure 4f) additional features appear. First, the maximum size differs by almost one order of magnitude depending on the Fo/(Fo+Melt) ratio, from 6.10^5 to 5.10^6 µm^3 with Fo/(Fo+Melt) ratio ranging from 70% to 90% respectively. Second, the volume fraction of the largest blob increases with the Fo/(Fo+Melt) ratio, from 1 to almost 10 vol%, which is likely a sign of localized interconnection. Variations of Fo/(Fo+Melt) ratio thus seem to have an effect only for relatively high metal fractions.

These observations of nickel textures at different scales seem to provide contradictory insights below the interconnection threshold of nickel: micro-scale textures and interfacial energy considerations imply that isolated nickel blobs should be spherical in all PC experiments studied here (Neri et al., 2019), but meso-scale textures indicate large irregular nickel blobs in a number of cases. Samples with such irregular blobs are thus inferred not to be far from textural equilibrium, as discussed in more detail below.

3.2.2 Time-resolved in-situ analysis

Ex-situ 3D microtomography only provides information on the final state of the experiments, but *in-situ* characterization of the samples allows to have time-resolved insight into the evolution of textural properties. Although these data highlight similar effects of varying silicate melt fraction as observed previously, complementary and critical information are also obtained to determine the evolution of the system from an initial post-compression state in which the sample has an extremely high solid/(solid+melt) ratio and irregular metallic textures, to a state approaching equilibrium (i.e. with macro-scale geometries consistent with grain-scale minimization of interfacial energies) at higher degree of melting, similar to the final state observed in PC experiments. As shown in Table 2, three PE experiments have been performed for the mixtures <65 : 25 : 10>, <70 : 5 : 25> and <65 : 5 : 30>.

We begin by illustrating the results for the low metal-content mixture <65 : 25 : 10>, concentrating on the characteristics of the largest blobs (Figure 5 insets 1-6 and Figure 6 in red). Just after compression and before heating of the <65 : 25 : 10> experiment (Figure 5 inset 1 and Figure 6a in red), the majority of the nickel is observed to be part of a single network, which represents 60-70 vol% of the total nickel. However, upon increasing temperature and silicate melt fraction, there is a radical change in behavior at 1950 K (well above nickel melting and the silicate eutectic), at which this network breaks apart (Figure 5 insets 3-4 and Figure 6a). Above this temperature the volume fraction of the largest nickel blob drops to 5 vol% and continues to decrease upon further heating until it reaches ≈ 1 vol% at 2080 K (Figure 5 insets 4-6 and Figure 6a). The NS (Figure 6b in red) shows a similar trend with a significant drop at the same temperature indicating that the network disruption forms blobs with shapes close to spherical (NS = 1). This effect is also qualitatively seen in 3D views of the 5 largest blobs (Figure 5 insets 1 to 6). Oscillations of the NS before its dramatic decrease indicate that the network is dynamic and constantly reorganizing itself, with local disruption and interconnection. This effect is illustrated by the positions of the second to fifth largest blobs that constantly change over the time of experiment

(Figure 5 insets 1 to 3).

NS populations and volume fraction distributions for all blobs of the <65 : 25 : 10> experiment are shown in Figure 7a and 7d respectively. NS populations indicate that a proportion of nickel blobs adopt highly non-spherical shapes (with cylinder equivalent aspect ratios that can exceed 1000) before the network breakdown (Figure 7a green and blue). After that point, nickel blobs become more and more spherical. For instance, at the highest temperature studied (2080 K, Figure 7a in red), the cylinder equivalent aspect ratios of the blobs barely exceed 10. The network breakdown induces two other important evolutions of the volume fraction and density distributions. The first one is the appearance of smaller blobs with maximum sizes decreasing from 10^6 to 10^5 μm^3 as temperature increases. On the other hand, blob growth occurs during the time of experiment, causing the loss of small blobs, within the range 10 to 10^3 μm^3. The combined effect of these two processes (network disruption and blob growth) narrows the range of volume fraction and density distributions, with a significant increase in the number of grains with volumes between 10^3 and 10^5 μm^3. At the end of the experiment, these distributions have exactly the same characteristics as those obtained from PC experiments with low metal contents or low Fo/(Fo+Melt) ratios (Figure 4a, 4b, 4d and 4e for mixtures with 10 and 15 Vol% of Ni): the maximum blob volume does not exceed 10^5 μm^3 and the largest blob does not represent much more than 1% of the total nickel in the sample. These observations thus provide evidence in favor of an initial distribution of nickel (generated by cold compression) that is not at equilibrium, as discussed in more details below.

For the PE experiments with 25 and 30 vol% of nickel, more than 99% of the total nickel content is part of a single large blob (Figure 5 insets 7-8 and Figure 6a in blue green and blue). This ubiquitous network is present from the beginning to the end of the experiment, with a volume fraction and a NS that are not subject to significant changes, even after Ni and eutectic-silicate melting. The NS of the largest blobs (Figures 6b, 7b and 7c) are high, between 75 and 100, corresponding to a cylinder equivalent aspect ratio of 10,000. The distributions in volume fraction (Figure 7e and 7f) are generally similar for the two mixtures (<70 : 5 : 25> and <65 : 5 : 30>) irrespective of temperature and silicate melt content. In detail, persistence of the metal network does not mean that there are no changes with temperature and time. For example, when the metal melts, there are local changes in texture. The surface area of contacts between metal and silicates decreases as the metallic liquid withdraws from spaces between grains that are too narrow, probably driven out by the wetting silicate liquid.

4. Discussion

4.1 Consequences of cold compression and the notion of interconnection threshold.

A notable feature of the results obtained *in-situ* is that a large proportion of metal grains already form an interconnected network below the onset of silicate and/or nickel melting. This is true even for the mixture of low metal proportion <65 : 25 : 10>. However, several lines of evidence suggest that this low temperature connectivity is not a persistent feature. The first is that the metal network is not global, representing only 60-70 vol% of the total Ni. Secondly, for the mixture <65 : 25 : 10>, the metal rapidly reorganizes itself at high temperature, disrupting the initial network. Thirdly, interconnection at 10 vol% of metal is incompatible with grain-scale equilibrium geometries of high dihedral angle. We thus conclude that initial connectivity results from the strains applied upon cold compression. Indeed, nickel is a "soft" phase that may be spread along grains of the harder silicate matrix by compression, thus forcing interconnection. Disruption of this forced network seems to require the metal be molten and to be favored by the presence of silicate melt. The detailed effects of temperature and

the fraction of silicate melt on the time required to disrupt the initial forced network cannot be assessed from this single experiment, but it is reasonable to assume that larger melt fractions will lead to faster disruption.

Concerning the mixtures of high metal fraction, (<70 : 5 : 25> and <65 : 5 : 30>) it is of note that the initial networks of metal grains cover > 99% of all Ni present and that the networks persist at all temperatures studied. This would indicate that an interconnected network of metal is a stable feature at these metal fractions. However, we note that in these experiments, the starting material contained 5 vol% of eutectic silicate melt, resulting in only 8-10 vol% of silicate melt at the end of the experiment. It is thus possible that the silicate melt fraction was insufficient to allow the metal network to reorganize and break apart. On the other hand, comparison with the *ex-situ* PC experiments indicates that melt fractions in this range *are* sufficient to disrupt metal networks formed by cold compression. For example, in runs with a Fo/(Fo+Melt) ratio of 90%, the silicate melt content is 9, 8.5 and 8 vol% for Ni contents of 10, 15 and 20 vol% respectively. All of these PC experiments show micro-textures largely dominated by isolated blobs at the end of the runs (Figure 3a-c). Note too that the PE experiments were kept at peak temperature for 4 hours in order to have a comparable thermal history to PC experiments. As such, the PE and PC experiments are complementary. Figure 3a-c and Figure 5 insets 7 and 8 thus constitute a series that illustrates variations in the evolution in the topology of metal for a constant Fo/(Fo+Melt) of ≈ 86% and metal content from 10 to 30 vol.%. In light of these considerations, the observed persistence of a connected network of Ni for metal content ≥ 25% in the PE experiments is taken to indicate that these experiments were above the stable nickel interconnection threshold in a partially molten silicate matrix.

Overall, these results highlight that care must be taken when defining the interconnection threshold, as the simple existence of a network of touching grains would not appear to be sufficient. The question then arises of how to assess if an observed network is persistent or not, and in the latter case, what are the factors controlling the timescale of network disruption. These issues will be treated below.

4.2 Processes responsible for textural maturation

Assuming that cold compression generates a forced interconnected network of metal grains at low temperature, the high interfacial energy of metal-silicate interfaces (see Section 3.1 and Néri et al., 2019) will provide a driving force for textural equilibration. However, such grain boundary migration requires atomic mobility and the timescales to reach a state of macroscopic equilibrium thus depend on pressure-temperature conditions and on the length scale of observation. In order to provide a relevant definition of the interconnection threshold, we must carefully consider the different mechanisms that can induce textural changes and their respective effects on the interconnectivity of the metallic phase.

Interfacial energies generate a pressure gradient along an interface, depending on its curvature. If only the metal is liquid, these pressure forces are unable to deform the silicate grains, but as soon as two liquids (silicate and metallic) are present, the interface between them can move and deform easily. The dynamics of this interface, also called Plateau-Rayleigh instability, depend on both inertial and viscous dissipation. The dimensionless Reynolds, Re, number provides the ratio between these terms and indicates which one prevails: $Re = \rho u L/\mu$, where ρ is the density of molten metal, μ its viscosity, u and L the characteristic velocity and length. The characteristic velocity is on the order of $u = \gamma/\mu$, with γ the surface tension between liquids, that is on the order of 1 Jm^{-2} (Keene, 1995). The viscosity of the most viscous fluid governs the dynamics of the interface. In the case of our experiments, Re remains well below one, indicating that inertial forces are negligible and that pressure gradients due to surface tensions are simply equilibrated by viscous dissipation. Under these conditions, an estimate

of the characteristic time for the displacement of the interface between the two liquids in the matrix can be derived from the velocity of a Poiseuille flow in a pipe (Aarts et al., 2005; Siggia, 1979): $u_p = \Delta p r^2/8\mu L$, such that $\tau = L/u_p = 4\mu L^2/\gamma r$, where Δp is the pressure difference, L the length of the pipe and r its radius. Considering a metallic film / pipe with a thickness / diameter of $2r \approx 10$ µm (derived from our microtomography data) and a length $L \approx 1$ mm (height of the sample), viscous dissipation will equilibrate the interface within 400 s. This timescale is much shorter than the disruption timescale observed (a few hours in our experiments), indicating that the disruption of the metallic network is not driven by the minimization of interfacial energies alone and that there is another, slower, limiting process. Nonetheless, minimization of interfacial energies may still be responsible for equilibration of micro-scale structures, such as triple junctions and metallic blobs trapped at silicate grain corners.

The most plausible explanation for observed network disruption is that the evolution of the metallic network is limited by the evolution of the shape of the solid silicate matrix. In other words, the nickel network is not disrupted instantaneously because the space between olivine grains cannot accommodate such rapid formation of disjointed metallic pockets. In other words, the shape of the metallic blobs is constrained by reorganization of the solid silicate matrix, textural evolution of metal grains or droplets following that of olivine grains, as previously proposed in silicate melt-free metal-silicate systems (Guignard et al., 2016, 2012). This hypothesis can be tested by comparing the evolution of the total surface area of metal blobs with that of silicate grains. The former is extracted from the 3D microtomography data, while the latter can only be estimated from grain growth laws for forsterite.

In a static environment (i.e. non-deforming), the evolution of olivine grain size is driven by Ostwald ripening:

$$a^n - a_0^n = ke^{-\frac{E}{RT}}t, \quad (2)$$

with a the grain size at time t, a_0 the initial grain size, n the growth law exponent that depends on the mechanism at work, k the growth rate, E the activation energy, R the gas constant and T the temperature. Considering that the number of grains of size a is inversely proportional to their individual volume a^3 while their individual surface area is proportional to a^2, it follows that the total grain surface area s is inversely proportional to their size. We can therefore write:

$$\frac{s(t)}{s_0} = \frac{a_0}{a(t)}, \quad (3)$$

where s_0 and a_0 are reference values for the total grain surface area and the grain size taken at the same time. Here, these reference values are initial values, right after compression.

Figure 8a displays the time evolution of the total surface area of the metal phase extracted from the 3D microtomography data and normalized to the initial value. It is compared with the total forsterite grain surface area (also normalized by the initial value) calculated from equation (3) and integration of equation (2) following the temperature evolution of the experimental system (shown as a black curve in Figure 8a). The parameters of the growth law are taken from Guignard et al. (2016, 2012) for the system with no silicate melt, and from (Guignard, 2011) above the eutectic temperature. The initial grain size is a free parameter for the integration of equation (2); the range 10-20 µm offers a good fit of the normalized surface area of metal phase - with 15 µm offering the best

fit - and is broadly consistent with the initial grain size of forsterite in the sample. Indeed, even if powders have been sieved to have an initial grain size larger than 30 µm, grains are likely to have been crushed during compression, thus reducing the starting grain size. The agreement between grain growth laws and experimental data shows that the dynamics of the liquid metal phase and the forsterite grain ripening share similar timescales. These data thus support the conclusion of Walte et al. (2007) and Bagdassarov et al. (2009) that textural maturation of high dihedral angle liquids is limited by the grain growth of the solid silicate matrix.

In light of these considerations, the interconnection threshold of a phase can thus be defined as the volume fraction at which an interconnected network persists in time, in the absence of external forces and at pressure-temperature conditions that permit grain-boundary movement (i.e. excluding kinetically arrested systems). For the system of study here, this interconnection threshold is derived to be between 20 and 25%. This value is broadly consistent with theoretical predictions made from measurements of dihedral angle at grain-boundary scale, which, for a two phase system, is on the order of ≈ 27 vol% (Wray, 1976).

4.3. Critical assessment of relevant interconnection thresholds of metal-rich liquids in a silicate matrix

Precise knowledge of the interconnection threshold is critical when addressing the question of metal-silicate differentiation in the early solar system. In natural systems, iron-rich melts are typically rich in sulfur too, the first-formed metal-rich liquids having a composition close to that of the Fe-FeS eutectic. Several studies have thus focused on the question of connectivity of a Fe-FeS eutectic liquid in a matrix of San Carlos olivine. However, even in this simple system various threshold values have been proposed, ranging from 3-6 vol% (Watson and Roberts, 2011; Yoshino et al., 2003) to 17.5 vol% (Bagdassarov et al., 2009). The discrepancy between values found for a single system at similar conditions, covering more than half of the total possible range of interconnection thresholds seriously complicates efforts to the numerical modeling of natural systems, as it is currently unclear which values are the most appropriate. Given that grain-growth of olivine has been determined to be a factor limiting textural equilibration in our experiments and that the same is to be expected for metal-sulphide melts, we will use our data to calculate time scales of textural equilibration (Figure 8b). This analysis will then be used to assess to what extent our data and that from the literature represent texturally equilibrated systems or not.

All our experiments were carried out with a significant fraction of a silicate melt, which strongly enhances grain growth (Guignard, 2011) and will reduce the time to reach textural maturation. The effect of the presence of silicate melt on olivine grain growth can be assessed using appropriate grain-growth laws, as illustrated in Figure 8b for a temperature of 1773 K corresponding to that of our PC experiments. For a system with silicate melt (Figure 8b, black curve), the normalized surface area calculated with an initial mean forsterite grain size of ≈ 15 µm starts to decrease within less than 1 hour and drops below 0.9 within four hours, an amplitude equivalent to that observed experimentally (Figure 8a) during the breakdown of the Ni network. Here, the thick solid line represents the evolution of the normalized surface area during the time of the experiment and the thin dashed line shows the predicted evolution for longer times than those studied experimentally. Performing the same calculation (same temperature and same initial grain size), but for a system with no silicate melt (Figure 8b, gray curve), it is predicted that it would take ≈ 10^2 hours for the normalized surface area to show a perceivable decrease and on the order of 10^3 hours to decrease by the amount observed in our partially molten system. The use of smaller grain sizes constitutes a way to decrease the timescales necessary for textural maturation, even in systems that do not contain silicate melt (Figure 8b, red curve). With this idea in mind, the model can be used to

calculate the maximum grain size that would result in disruption of the initial forced network within 4 hours at silicate subsolidus conditions. The corresponding value is ≈ 5 µm. Given that grain growth is a thermally activated process, the situation is even worse at lower temperature. For example, just below the eutectic temperature of natural systems (≈ 1270 K), the calculations indicate that even for an initial grain size of ≈ 2 µm, about one year would be necessary to observe the disruption of forced metal networks generated during cold compression.

The same reasoning can be applied to critically reanalyze literature data in the San Carlos olivine - Fe-FeS eutectic system, in particular the role of initial grain-size and experimental conditions (i.e. temperature). Yoshino et al. (2003) used San Carlos olivine powder with a mean grain size of 10-20 µm and equilibrated the samples for 20 hours at 1573 K (Figure 8b, green curve), while Roberts et al. (2007) and Watson and Roberts (2011) used a starting grain size of 45 µm, temperature in the range 1573-1623 K and run durations of 24 hours (Figure 8b, blue curve). Using grain growth laws of olivine grains in presence of an iron-sulfide melt (Solferino et al., 2015; Solferino and Golabek, 2018), the evolution of the normalized total surface area shows no decrease during the time of experiment (Figure 8b, full green and blue curves). At these conditions, the model predicts that the evolution of the normalized surface area (and associated break up of the forced network) requires thousands of hours for experiments of Yoshino et al. (2003) (Figure 8b green dashed line) and ≈ 10^7 hours (i.e. ≈ 1 kyr) for the experiments of Roberts et al. (2007) and Watson and Roberts (2011). Hence, we conclude that textural maturation is not likely to have been approached in these experiments. Bagdassarov et al. (2009) on the other hand had identified that the use of such large initial grain sizes hindered the approach of textural equilibrium and consequently used initial grain sizes of 1.8 µm. At 1373 K and in the absence of silicate melt (Figure 8b, red curve), our calculations indicate that the normalized total surface area starts to decrease extremely rapidly, decreasing far below the value of 0.9 during the time of experiment. Based upon this analysis, it can be surmised that the interconnection threshold proposed by Yoshino et al. (2003), Roberts et al. (2007) and Watson and Roberts (2011) were obtained far from textural equilibrium and may be underestimated. The case has been made that the threshold values of Yoshino et al. (2003), Roberts et al. (2007) and Watson and Roberts (2011)correspond to the theoretical value (calculated using Wray, 1976) for the regular assemblage of truncated octahedral (tetrakaidecahedron) crystals. However, Ghanbarzadeh et al. (2017) show that this threshold is sensitive to grain shape. On irregular polycrystalline material, such as a natural or experimental samples, the threshold is significantly higher than that determined on idealized grains (truncated octahedra). For example, for a dihedral angle of 110°, as in the case of contacts between olivine and Fe-FeS eutectic metal, Ghanbarzadeh et al. (2017) find a threshold close to that determined by Bagdassarov et al. (2009). Ghanbarzadeh et al. (2017) also indicate that "*textural equilibrium allows multiple solutions that represent local minima in interfacial energy*", so that the threshold required to achieve connectivity is higher than that at which the connectivity is broken by metal drainage. The latter values are then close to the theoretical thresholds. The authors explain this change by the continuous phase rearrangement during drainage that always occurs at textural equilibrium in their simulations. While this hysteresis has important implications to estimate the fraction of metal that can be drained or trapped in a natural sample undergoing Fe-FeS melting (e.g. Néri et al., 2019), it cannot be invoked to explain the low threshold values reported by Yoshino et al. (2003), Roberts et al. (2007) and Watson and Roberts (2011). Our analysis rather suggests that the real threshold is closer to the estimate of Bagdassarov et al. (2009).

4.4 Textures in natural samples

While grain-size can lead to the preservation of forced textures in experimental systems (e.g. those produced

by cold compression), the time-scales of natural systems (> 1Ma) will favor an approach to equilibrium, even in melt-free systems (i.e. ordinary chondrites). In this final section, textures of meteorites that experienced increasing peak temperatures will be used to shed light on the processes that affected such natural systems formed in the early solar system.

Chondrules can be considered as one endmember as they experienced high peak temperature (T_{peak} ≈ 1773-1873 K) in the presence of a significant amount of silicate melt (e.g. Zanda, 2004). In this respect, our PC experiments constitute a good analogue and we note that both chondrules and our metal-rich experiments exhibit similar textures with iron-rich phases being close to perfectly spherical. At the other extreme, H4 chondrites experienced low peak temperature (T_{peak} ≈ 800 K) (Guignard et al., 2016; Monnereau et al., 2013), thus evolved in a melt-free system, whether silicate or metal-sulfide. In these samples, iron-rich phases are fine-grained minerals homogeneously distributed in a matrix of grains with irregular shapes. Objects that experienced intermediate peak temperatures with no melt present are H5 (T_{peak} ≈ 1100 K) and H6 (T_{peak} ≈ 1200 K, Guignard et al., 2016 and Monnereau et al., 2013) while the primitive achondrites, i.e. acapulcoites (T_{peak} ≈ 1373 K, Palme et al., 1981) and lodranites (T_{peak} ≈ 1473 K, McCoy et al., 1997) show evidence for melting of the metal-sulfide and silicate subsystems.

To explore the consequences of these different conditions on metal textures, we have quantified the shape of metal-rich phases in samples of the above-mentioned suite of meteorites. For simplicity, we concentrate here on the degree of 2D non-circularity ΔC (see Guignard and Toplis, 2015) derived from images obtained by SEM or optical microscopy. The parameter ΔC is defined as:

$$\Delta C(\%) = \frac{(P_m - 2\pi R_{eff})}{P_m} \times 100 \quad (4)$$

where P_m is the measured perimeter of a grain and R_{eff} is the radius of the circle corresponding to the measured area of the grain A_m, calculated as:

$$R_{eff} = \sqrt{\frac{A_m}{\pi}} \quad (5)$$

Data for the degree of non-circularity of iron-rich phases originate from different sources. H-chondrite data were taken from Guignard and Toplis (2015) and data for chondrules were calculated from pictures of Ganino et al. (2019), with permission from the authors. Finally, data for acapulcoites and lodranites were acquired from optical micrographs of sections of Acapulco and Lodran (sections Acapulco -2 and Lodran ns 2 respectively) loaned by the Museum National d'Histoire Naturelle (MNHN, Paris).

Textures of the iron-rich phases in this suite of natural objects are shown in Figure 9 and Figure 10 which represent the ΔC distributions. Textural maturation is limited by grain growth processes, which are controlled by thermal history (mostly peak temperature and time spent at this temperature) and the presence or absence of silicate melt. On the one hand, chondrules show a peak frequency at ΔC ≈ 3%, indicating extremely rounded metallic grains. Based on equation (3), textural maturation is extremely fast (< 10 minutes), a feature matching the extremely short and intense thermal history of chondrules. On the other hand, H chondrites span a wide range of non-circularity, from ΔC ≈ 50% for petrologic type H4 to ΔC ≈ 10-15% for petrologic type H6 (Guignard and Toplis, 2015). These values are consistent with subsolidus conditions and low peak temperatures. In the H chon-

drite series, samples of H4 display the least rounded metallic grains because their low peak temperature requires timescales of a billion years to have significant grain growth, while the longer thermal history and higher peak temperature of H6 (Guignard et al., 2016; Monnereau et al., 2013) led to metallic grains that are more rounded. Acapulco and Lodran experienced peak temperatures intermediate between petrologic type H6 and chondrules and show signs of partial melting (Keil and McCoy (2018) and references therein), thus their ΔC distribution is expected to be intermediate between these objects. However, these primitive achondrites are found to have non-circularity values between the least texturally mature samples: petrologic types H4 and H5 (Figure 10), indicating textures that are out of equilibrium and highlighting a process that forced and maintained these textural properties.

For acapulcoites and lodranites, such process can be the migration of the silicate melt that may have induced the compaction of the matrix, applying a strain on iron-rich phases and forcing them to adopt shapes that deviate from the equilibrated sphere. In this respect, samples of Acapulco and Lodran may have experienced the same sort of compaction as the cold compression of our experiments – most likely to a lesser extent – that forces metallic grains to deform and adopt shapes that are highly non-spherical. Although these objects were maintained at relatively high temperature for long periods of time (a few million years, e.g. Neumann et al., 2018), textural changes were inefficient and the iron-rich phases did not adopt spherical shapes. This feature is most likely due to limited grain boundary mobility after melt extraction - as revealed by the huge difference in growth rate of silicate between solid and partially molten system (Guignard, 2011; Guignard et al., 2016, 2012) - and the relatively large grain sizes acquired in the presence of silicate melt. Indeed, once grains grow up to a few hundred microns in partially molten conditions, as in acapulcoites and lodranites (Keil and McCoy (2018) and references therein), further significant grain growth after the removal of the silicate melt requires more than 10 Myr. This timescale is similar to that necessary for textural maturation after compaction, following equation (3), but is larger than the peak temperature lifetime of the acapulcoite-lodranite parent body (Neumann et al., 2018). Hence, the extraction of silicate melt caused the "freezing" of both silicate grain size and irregular textures of iron-rich phases.

The removal of the silicate melt not only affected the textural properties of iron-rich phases but also the differentiation history of the parent body through the formation of a forced Fe-FeS melt network, as shown here. Most studies of metal-silicate differentiation in primitive achondrites have assumed a low interconnection threshold of the Fe-FeS eutectic melt (Néri et al., 2019; Neumann et al., 2018, 2012; Šrámek et al., 2012), on the order of 3 vol% (Roberts et al., 2007; Watson and Roberts, 2011; Yoshino et al., 2003). However, such a low value seems to be the result of poorly equilibrated sample textures, yielding an underestimate of the value required to have a stable interconnected network (see Section 4.3 and Bagdassarov et al. (2009)). Assuming equilibrated textures in a planetesimal and using interconnection threshold values in such conditions (e.g. 17.5 vol% for the Fe-FeS eutectic composition, Bagdassarov et al. 2009), no persistent networks could be formed during the evolution history of lodranites. Indeed, considering that primitive achondrites originate from precursor material with a composition close to that of H chondrites (Palme et al., 1981), i.e. a modal fraction of iron-rich phases of $\approx$ 10 vol% (Guignard and Toplis, 2015), interconnection cannot be achieved unless the silicate partial melt is extracted, and even so, such high threshold values require the removal of 40-50 vol% of the silicates. This degree of melting is way above the geochemical and petrological constraints on lodranites (20 vol%, McCoy et al., 1997), precluding the formation of a stable interconnected network in their parent body. However, new pathways

are opened if forced interconnectivity is considered. Indeed, the assumption of continuous extraction of a silicate melt as proposed in Néri et al. (2019) can be reconciled with the experimental data presented here if one assumes that continuous compaction of the matrix forces disequilibrium geometries and interconnection. Although the extraction of 20 vol% of silicate melt (i.e. that derived for lodranites), would only increase the iron-sulfur melt fraction to ≈ 5 vol% (estimated from Néri et al. (2019)), previous studies of Yoshino et al. (2003), Roberts et al. (2007) and Watson and Roberts (2011) indicate that such a fraction is enough to force the interconnectivity of a Fe-FeS melt. Whether or not such a forced network exists in these natural samples could be resolved by the use of 3D X-ray microtomography on the main masses of these meteorites, but even if connected, this will not answer the question of whether such a forced network is able to percolate over relevant time-scales. More experimental efforts are required to shed light on this point.

5. Conclusion

Experiments were performed to determine the influence of different parameters on the interconnection threshold of pure metal in a partially molten silicate matrix of relevance to metal-silicate differentiation processes in small rocky bodies of the early solar system. Overall, the main conclusions can be summarized as follows:

(1) Comparison between grain-scale and sample-scale textural properties indicates that large-scale textural equilibrium is not always reached. Indeed, measured dihedral angles indicate that nickel grains should be approximately spherical at equilibrium. However, macroscopic properties of nickel determined from 3D X-Ray microtomography reveal blobs with irregular shapes that largely differ from the organization expected for equilibrium. The degree of textural maturation depends on the relative contents of the different phases. The most equilibrated textures are produced in samples bearing large contents of silicate melt and a low nickel fraction.

(2) The connectivity of the metal in experimental charges may result from cold compression even when the metal content is lower than its interconnection threshold. Time-resolved *in-situ* 3D X-Ray microtomography indicates that nickel gets squeezed between silicate grains and forms a network before melting begins. However, once this metallic network and a fraction of silicates are molten, the forced network of metal grains is disrupted into smaller units, which eventually become spheres as a result of the minimization of interfacial energies.

(3) The disruption of the forced network generated during compression occurs on a timescale of a few hours and can be explained by grain growth of the solid silicate matrix, as already suggested by Walte et al. (2007) and Bagdassarov et al. (2009). The interconnection threshold can thus be defined as the phase fraction at which a network of touching grains exists, adding that this network must persist in time in the absence of external forces and at pressure-temperature conditions that permit grain-boundary movement (i.e. excluding kinetically arrested systems). Using this definition, the interconnection threshold of pure nickel in a partially molten silicate matrix lies between 20 and 25 vol%. Interconnection threshold values for Fe-FeS eutectic compositions proposed in the literature are reviewed and it is concluded that many of them are likely to be underestimated.

(4) Natural objects display iron and troilite grains that range in shape from almost spherical to highly irregular. In chondrules, metal grains are largely spherical because they were once molten in the presence of significant amounts of silicate melt. Hence, these objects experienced efficient textural maturation, allowing the iron and troilite pools to form spheres rapidly. On the contrary, irregular metallic grains characterize primitive achondrites. This can be explained by the extraction of a silicate melt and compaction of the silicate matrix, leading to iron and troilite beads being constrained to occupy the available place between silicate crystals. Once the liquid

has been extracted, grain boundary migration is hindered and subsequent textural maturation occurs on time-scales longer than the peak temperature lifetime of these objects, freezing irregular textures.

Acknowledgements

We wish to thank Ken Koga and Didier Laporte (LMV, Université Clermont-Auvergne, Clermont-Ferrand, France) for helpful discussions and assistance on piston-cylinder assemblies and experiments, and Philippe de Parseval and Sophie Gouy, Stéphane le Blond du Plouy and Arnaud Proietti (Centre Raimond Castaing, Toulouse, France) for EMPA analyses, SEM imaging and EBSD analyses, respectively. We are very grateful to MNHN (Paris, France) for the loan of thick sections of Acapulco and Lodran (colhelper number 100951), and to Guy Libourel for providing us images of chondrules. This work is part of the PALLAS project funded by the ANR (grant ANR-14-CE33-006-01 to G. Quitté); we also thank the Université Paul Sabatier for its contribution to the PhD grant to A. Néri. SOLEIL Synchrotron as well as PSICHE beamline teams are acknowledged for beamtime allocation following proposal number 20180672.

References

Aarts, D.G.A.L., Dullens, R.P.A., Lekkerkerker, H.N.W., 2005. Interfacial dynamics in demixing systems with ultralow interfacial tension. New J. Phys. 7, 40–40. https://doi.org/10.1088/1367-2630/7/1/040

Anderson, J.D., Lau, E.L., Sjorgren, W.L., Schubert, G., Moore, W.B., 1996. Gravitational constraints on the internal structure of Ganymede. Nature 384, 541–543. https://doi.org/10.1038/384541a0

Bagdassarov, N., Golabek, G.J., Solferino, G., Schmidt, M.W., 2009. Constraints on the Fe-S melt connectivity in mantle silicates from electrical impedance measurements. Phys. Earth Planet. Inter. 177, 139–146. https://doi.org/10.1016/j.pepi.2009.08.003

Ballhaus, C., Ellis, D.J., 1996. Mobility of core melts during Earth's accretion. Earth Planet. Sci. Lett. 143, 137–145. https://doi.org/10.1016/0012-821X(96)00135-5

Bild, R.W., Wasson, J.T., 1976. The Lodran meteorite and its relationship to the ureilites. Mineral. Mag. 40, 721–735. https://doi.org/10.1180/minmag.1976.040.315.06

Boulard, E., Denoual, C., Dewaele, A., King, A., Le Godec, Y., Guignot, N., 2020. Following the phase transitions of iron in 3D with X-ray tomography and diffraction under extreme conditions. Acta Mater. 192, 30–39. https://doi.org/10.1016/j.actamat.2020.04.030

Boulard, E., King, A., Guignot, N., Deslandes, J.-P., Le Godec, Y., Perrillat, J.-P., Clark, A., Morard, G., Itié, J.-P., 2018. High-speed tomography under extreme conditions at the PSICHE beamline of the SOLEIL Synchrotron. J. Synchrotron Radiat. 25, 818–825. https://doi.org/10.1107/s1600577518004861

Bulau, J.R., Waff, H.S., Tyburczy, J.A., 1979. Mechanical and thermodynamic constraints on fluid distribution in partial melts. J. Geophys. Res. Solid Earth 84, 6102–6108. https://doi.org/10.1029/JB084iB11p06102

Buono, A.S., Walker, D., 2011. The Fe-rich liquidus in the Fe–FeS system from 1bar to 10GPa. Geochim. Cosmochim. Acta 75, 2072–2087. https://doi.org/10.1016/j.gca.2011.01.030

Chabot, N.L., Haack, H., 2006. Evolution of Asteroidal Cores, in: Meteorites and the Early Solar System II. University of Arizona Press, pp. 747–771.

Cmíral, M., Gerald, J.D.F., Faul, U.H., Green, D.H., 1998. A close look at dihedral angles and melt geometry in olivine-basalt aggregates: a TEM study. Contrib. to Mineral. Petrol. 130, 336–345. https://doi.org/10.1007/s004100050369

Crichton, W., Mezouar, M., 2002. Noninvasive pressure and temperature estimation in large-volume apparatus by equation-of-state cross-calibration. High Temp. Press. 34, 235–242. https://doi.org/10.1068/htjr019

Eliceiri, K., Schneider, C.A., Rasband, W.S., Eliceiri, K.W., 2012. NIH Image to ImageJ : 25 years of image analysis. Nat. Methods 9, 671–675. https://doi.org/10.1038/nmeth.2089

Faul, U.H., 2000. Constraints on the Melt Distribution in Anisotropic Polycrystalline Aggregates Undergoing Grain Growth, in: Bagdassarov, N., Laporte, D., Thompson, A.B. (Eds.), Physics and Chemistry of Partially Molten Rocks. Springer Netherlands, Dordrecht, pp. 67–92. https://doi.org/10.1007/978-94-011-4016-4_3

Gaetani, G.A., Grove, T.L., 1999. Wetting of mantle olivine by sulfide melt: implications for Re/Os ratios in mantle peridotite and late-stage core formation. Earth Planet. Sci. Lett. 169, 147–163. https://doi.org/10.1016/S0012-821X(99)00062-X

Ganino, C., Libourel, G., Nakamura, A.M., Michel, P., 2019. Are hypervelocity impacts able to produce chondrule-like ejecta? Planet. Space Sci. 177, 104684. https://doi.org/10.1016/j.pss.2019.06.008

Ghanbarzadeh, S., Hesse, M.A., Prodanović, M., 2017. Percolative core formation in planetesimals enabled by hysteresis in metal connectivity. Proc. Natl. Acad. Sci. 114, 13406–13411. https://doi.org/10.1073/pnas.1707580114

Goldstein, J.I., Scott, E.R.D., Chabot, N.L., 2009. Iron meteorites: Crystallization, thermal history, parent bodies, and origin. Chemie der Erde 69, 293–325. https://doi.org/10.1016/j.chemer.2009.01.002

Greenwood, R.C., Barrat, J.-A., Yamaguchi, A., Franchi, I.A., Scott, E.R.D., Bottke, W.F., Gibson, J.M., 2014. The oxygen isotope composition of diogenites: Evidence for early global melting on a single, compositionally diverse, HED parent body. Earth Planet. Sci. Lett. 390, 165–174. https://doi.org/10.1016/j.epsl.2013.12.011

Guignard, J., 2011. Caractérisation texturale des assemblages Métal-Silicate lors de la différenciation des planétésimaux : Etude de météorites & Approche expérimentale. Université Toulouse III Paul Sabatier.

Guignard, J., Bystricky, M., Toplis, M.J., 2012. Grain growth in forsterite-nickel mixtures: Analogues of small parent bodies during early accretion. Phys. Earth Planet. Inter. 204–205, 37–51. https://doi.org/10.1016/j.pepi.2012.06.002

Guignard, J., Toplis, M.J., 2015. Textural properties of iron-rich phases in H ordinary chondrites and quantitative links to the degree of thermal metamorphism. Geochim. Cosmochim. Acta 149, 46–63. https://doi.org/10.1016/j.gca.2014.11.006

Guignard, J., Toplis, M.J., Bystricky, M., Monnereau, M., 2016. Temperature dependent grain growth of forsterite-nickel mixtures: Implications for grain growth in two-phase systems and applications to the H-chondrite parent body. Earth Planet. Sci. Lett. 443, 20–31. https://doi.org/10.1016/j.epsl.2016.03.007

Holzheid, A., Schmitz, M.D., Grove, T.L., 2000. Textural equilibria of iron sulfide liquids in partly molten silicate aggregates and their relevance to core formation scenarios. J. Geophys. Res. Solid Earth 105, 13555–13567. https://doi.org/10.1029/2000JB900046

Jurewicz, S.R., Watson, E.B., 1985. The distribution of partial melt in a granitic system: The application of liquid phase sintering theory. Geochim. Cosmochim. Acta 49, 1109–1121. https://doi.org/10.1016/0016-7037(85)90002-X

Keene, B.J., 1995. Interfacial tension between ferrous melts and molten slags, in: Dusseldorf : Verlag Stahleisen GmbH cop. 1995 (Ed.), Slag Atlas / Edited by Verein Deutscher Eisenhuttenleute (VDEh). - 2nd Edition. pp. 463–511.

Keil, K., McCoy, T.J., 2018. Acapulcoite-lodranite meteorites: Ultramafic asteroidal partial melt residues. Geochemistry 78, 153–203. https://doi.org/10.1016/j.chemer.2017.04.004

Ketcham, R.A., 2005. Computational methods for quantitative analysis of three-dimensional features in geological specimens. Geosphere 1, 32. https://doi.org/10.1130/GES00001.1

Kivelson, M.G., Khurana, K.K., Russell, C.T., Walker, R.J., Warnecke, J., Coroniti, F. V., Polanskey, C., Southwood, D.J., Schubert, G., 1996. Discovery of Ganymede's magnetic field by the Galileo spacecraft. Nature 384, 537–541. https://doi.org/10.1038/384537a0

Laporte, D., Provost, A., 2000. The Grain Scale Distribution of Silicate, Carbonate and Metallosulfide Partial Melts: a Review of Theory and Experiments, in: Bagdassarov, N., Laporte, D., Thompson, A.B. (Eds.), Physics and Chemistry of Partially Molten Rocks. Springer Netherlands, pp. 93–140. https://doi.org/10.1007/978-94-011-4016-4_4

Le Godec, Y., Martinez-Garcia, D., Mezouar, M., Syfosse, G., Itié, J.-P., Besson, J.-M., 2000. Thermoelastic behaviour of hexagonal graphite-like boron nitride. High Press. Res. 17, 35–46. https://doi.org/10.1080/08957950008200304

McCoy, T.J., Keil, K., Clayton, R.N., Mayeda, T.K., Bogard, D.D., Garrison, D.H., Huss, G.R., Hutcheon, I.D., Wieler, R., 1996. A petrologic, chemical, and isotopic study of Monument Draw and comparison with other acapulcoites: Evidence for formation by incipient partial melting. Geochim. Cosmochim. Acta 60, 2681–2708. https://doi.org/10.1016/0016-7037(96)00109-3

McCoy, T.J., Keil, K., Clayton, R.N., Mayeda, T.K., Bogard, D.D., Garrison, D.H., Wieler, R., 1997. A petrologic and isotopic study of lodranites: Evidence for early formation as partial melt residues from heterogeneous precursors. Geochim. Cosmochim. Acta 61, 623–637. https://doi.org/10.1016/S0016-7037(96)00359-6

Minarik, W.G., Ryerson, F.J., Watson, E.B., 1996. Textural Entrapment of Core-Forming Melts. Science (80-.). 272, 530–533. https://doi.org/10.1126/science.272.5261.530

Mirone, A., Brun, E., Gouillart, E., Tafforeau, P., Kieffer, J., 2014. The PyHST2 hybrid distributed code for high speed tomographic reconstruction with iterative reconstruction and a priori knowledge capabilities. Nucl. Instruments Methods Phys. Res. Sect. B Beam Interact. with Mater. Atoms 324, 41–48. https://doi.org/10.1016/j.nimb.2013.09.030

Mittlefehldt, D.W., Lindstrom, M.M., Bogard, D.D., Garrison, D.H., Field, S.W., 1996. Acapulco- and Lodran-like achondrites: Petrology, geochemistry, chronology, and origin. Geochim. Cosmochim. Acta 60, 867–881. https://doi.org/10.1016/0016-7037(95)00423-8

Monnereau, M., Toplis, M.J., Baratoux, D., Guignard, J., 2013. Thermal history of the H-chondrite parent body: Implications for metamorphic grade and accretionary time-scales. Geochim. Cosmochim. Acta 119, 302–321. https://doi.org/10.1016/j.gca.2013.05.035

Néri, A., Guignard, J., Monnereau, M., Toplis, M.J.J., Quitté, G., 2019. Metal segregation in planetesimals: Constraints from experimentally determined interfacial energies. Earth Planet. Sci. Lett. 518, 40–52. https://doi.org/10.1016/j.epsl.2019.04.049

Neumann, W., Breuer, D., Spohn, T., 2012. Differentiation and core formation in accreting planetesimals. a&a 543. https://doi.org/10.1051/0004-6361/201219157

Neumann, W., Henke, S., Breuer, D., Gail, H.-P., Schwarz, W.H., Trieloff, M., Hopp, J., Spohn, T., 2018. Modeling the evolution of the parent body of acapulcoites and lodranites: A case study for partially differentiated asteroids. Icarus 311, 146–169. https://doi.org/10.1016/j.icarus.2018.03.024

Paganin, D., Mayo, S.C., Gureyev, T.E., Miller, P.R., Wilkins, S.W., 2002. Simultaneous phase and amplitude extraction from a single defocused image of a homogeneous object. J. Microsc. 206, 33–40. https://doi.org/10.1046/j.1365-2818.2002.01010.x

Palme, H., Schultz, L., Spettel, B., Weber, H.., Wänke, H., Michel-Levy, M.C., Lorin, J.., 1981. The Acapulco meteorite: Chemistry, mineralogy and irradiation effects. Geochim. Cosmochim. Acta 45, 727–752. https://doi.org/10.1016/0016-7037(81)90045-4

Papike, J.J., Spilde, M.N., Fowler, G.W., Layne, G.D., Shearer, C.K., 1995. The Lodran primitive achondrite: petrogenetic insights from electron and ion microprobe analysis of olivine and orthopyroxene. Geochim. Cosmochim. Acta 59, 3061–3070. https://doi.org/10.1016/0016-7037(95)00195-6

Patzer, A., Hill, D.H., Boynton, W. V., 2004. Evolution and classification of acapulcoites and lodranites from a chemical point of view. Meteorit. Planet. Sci. 39, 61–85. https://doi.org/10.1111/j.1945-5100.2004.tb00050.x

Presnall, D.C., Dixon, S.A., Dixon, J.R., O'Donnell, T.H., Brenner, N.L., Schrock, R.L., Dycus, D.W., 1978. Liquidus phase relations on the join diopside-forsterite-anorthite from 1 atm to 20 kbar: Their bearing on the generation and crystallization of basaltic magma. Contrib. to Mineral. Petrol. 66, 203–220. https://doi.org/10.1007/BF00372159

Righter, K., 2002. Does the Moon Have a Metallic Core? Constraints from Giant Impact Modeling and Siderophile Elements. Icarus 158, 1–13. https://doi.org/10.1006/icar.2002.6859

Roberts, J.J., Kinney, J.H., Siebert, J., Ryerson, F.J., 2007. Fe-Ni-S melt permeability in olivine: Implications for planetary core formation. Geophys. Res. Lett. 34, L14306. https://doi.org/10.1029/2007GL030497

Rose, L.A., Brenan, J.M., 2001. Wetting Properties of Fe-Ni-Co-Cu-O-S Melts against Olivine: Implications for Sulfide Melt Mobility. Econ. Geol. 96, 145–157. https://doi.org/10.2113/gsecongeo.96.1.145

Schindelin, J., Arganda-Carreras, I., Frise, E., Kaynig, V., Longair, M., Pietzsch, T., Preibisch, S., Rueden, C., Saalfeld, S., Schmid, B., Tinevez, J.-Y., White, D.J., Hartenstein, V., Eliceiri, K., Tomancak, P., Cardona, A., 2012. Fiji: an open-source platform for biological-image analysis. Nat. Methods 9, 676–682. https://doi.org/10.1038/nmeth.2019

Schubert, G., Zhang, K., Kivelson, M.G., Anderson, J.D., 1996. The magnetic field and internal structure of Ganymede. Nature 384, 544–545. https://doi.org/10.1038/384544a0

Shannon, M.C., Agee, C.B., 1996. High pressure constraints on percolative core formation. Geophys. Res. Lett. 23, 2717–2720. https://doi.org/10.1029/96GL02817

Siggia, E.D., 1979. Late stages of spinodal decomposition in binary mixtures. Phys. Rev. A 20, 595–605. https://doi.org/10.1103/PhysRevA.20.595

Smith, C.S., 1964. Some elementary principles of polycrystalline microstructure. Metall. Rev. 9, 1–48. https://doi.org/10.1179/mtlr.1964.9.1.1

Solferino, G.F.D., Golabek, G.J., 2018. Olivine grain growth in partially molten Fe–Ni–S: A proxy for the genesis of pallasite meteorites. Earth Planet. Sci. Lett. 504, 38–52. https://doi.org/10.1016/j.epsl.2018.09.027

Solferino, G.F.D., Golabek, G.J., Nimmo, F., Schmidt, M.W., 2015. Fast grain growth of olivine in liquid Fe-S and the formation of pallasites with rounded olivine grains. Geochim. Cosmochim. Acta 162, 259–275. https://doi.org/10.1016/j.gca.2015.04.020

Šrámek, O., Milelli, L., Ricard, Y., Labrosse, S., 2012. Thermal evolution and differentiation of planetesimals and planetary embryos. Icarus 217, 339–354. https://doi.org/10.1016/j.icarus.2011.11.021

Strong, H.M., Bundy, F.P., 1959. Fusion Curves of Four Group VIII Metals to 100 000 Atmospheres. Phys. Rev. 115, 278–284. https://doi.org/10.1103/PhysRev.115.278

Walte, N.P., Becker, J.K., Bons, P.D., Rubie, D.C., Frost, D.J., 2007. Liquid-distribution and attainment of textural equilibrium in a partially-molten crystalline system with a high-dihedral-angle liquid phase. Earth Planet. Sci. Lett. 262, 517–532. https://doi.org/10.1016/j.epsl.2007.08.003

Watson, H.C., Roberts, J.J., 2011. Connectivity of core forming melts: Experimental constraints from electrical conductivity and X-ray tomography. Phys. Earth Planet. Inter. 186, 172–182.

https://doi.org/10.1016/j.pepi.2011.03.009
Wray, P.., 1976. The geometry of two-phase aggregates in which the shape of the second phase is determined by its dihedral angle. Acta Metall. 24, 125–135. https://doi.org/10.1016/0001-6160(76)90015-8
Yoshino, T., Walter, M.J., Katsura, T., 2003. Core formation in planetesimals triggered by permeable flow. Nature 422, 154–157. https://doi.org/10.1038/nature01459
Zanda, B., 2004. Chondrules. Earth Planet. Sci. Lett. 224, 1–17. https://doi.org/10.1016/j.epsl.2004.05.005
Zha, C.-S., Mibe, K., Bassett, W.A., Tschauner, O., Mao, H.-K., Hemley, R.J., 2008. P-V-T equation of state of platinum to 80GPa and 1900K from internal resistive heating/x-ray diffraction measurements. J. Appl. Phys. 103, 054908. https://doi.org/10.1063/1.2844358
Zipfel, J., Palme, H., Kennedy, A.K., Hutcheon, I.D., 1995. Chemical composition and origin of the Acapulco meteorite. Geochim. Cosmochim. Acta 59, 3607–3627. https://doi.org/10.1016/0016-7037(95)00226-P

Table 1: Compositions in wt% of the synthesized silicate melts in the Anorthite-Diopside-Forsterite (An-Di-Fo) ternary diagram. Composition of the synthesized silicate glasses were determined by Electron MicroProbe Analyses (EMPA) based on repeated measurements on at least 30 points. Results correspond to the desired composition within 1 wt%.

Phase composition (wt%)	An	Di	Fo	CaO	MgO	Al_2O_3	SiO2
Glass in eq. with Fo at 1773 K at 1 GPa	51.9	20.0	28.9	14.55	22.92	17.04	45.59
1 GPa eutectic	52	30	18	18.25	15.9	19.06	46.79

Table 2: Initial phase proportions, experimental conditions and voxel sizes of the 3D X-Ray microtomography analyses for the different experiments. Proportions are expressed as forsterite (Fo) : silicate melt (Melt) : nickel (Ni) in volume percent. PC is for the piston-cylinder experiments and PE for the Paris-Edinburgh press experiments. Numbers in parentheses correspond to the uncertainty in the silicate melt content calculated from the errors on temperature determination.

Fo:Melt:Ni (vol%)	Set up	Silicate melt content	Pressure (GPa)	Temperature (K)	Time	Voxel size (µm)
81 : 9 : 10	PC	Constant	1	1773	4 h	1.75
76.5 : 8.5 : 15	PC	Constant	1	1773	4 h	1.50
68 : 17 : 15	PC	Constant	1	1773	4 h	1.80
59.5 : 25.5 : 15	PC	Constant	1	1773	4 h	1.50
72 : 8 : 20	PC	Constant	1	1773	4 h	1.67
64 : 16 : 20	PC	Constant	1	1773	4 h	1.80
56 : 24 : 20	PC	Constant	1	1773	4 h	1.70
65 : 25 : 10	PE	25 – 75(5)	1	300 to 2123	8 h	1.30
70 : 5 : 25	PE	5 – 8(2)	1	300 to 1823	7 h	1.30
65 : 5 : 30	PE	5 – 10(2)	1	300to 1973	8 h	1.30

Figure 1: Assemblies used for the experiments conducted in this study. (a) Piston-cylinder assembly. Samples are encapsulated in graphite capsules and placed in the hot-zone of the furnace with MgO spacers. Temperature is monitored and controlled using a type C thermocouple (± 5 K). (b) Paris-Edinburgh press assembly. A double capsule is used, the inner one made of graphite and the outer one made of boron nitride to isolate the

inner capsule from the furnace. No thermocouple can be used in this setup as the sample must be able to rotate freely for the 3D X-Ray microtomography measurements. Hence, temperature and pressure are calculated with the cross-calibration method, using a mixture of platinum and boron nitride powders (Crichton and Mezouar, 2002; Le Godec et al., 2000; Zha et al., 2008).

Figure 2: High resolution SEM images (30 nm per pixel) showing typical micro-textures of the PC experiments. (a) SEM image of the <76.5 : 8.5 : 15> (<Fo : Melt : Ni>) mixture and (b) SEM image of the <72 : 8 : 20> one. Nickel appears in white, silicate melt in light grey and forsterite in dark grey. Micro-textures show a strong non-wetting behavior of the nickel pools, while the silicate melt is highly wetting. Dihedral measurements on such images yield similar values to Néri et al. (2019) within error bars.

Figure 3: 3D view of the five largest nickel blobs of the recovered PC samples (4h at 1773K, see Table 2 for compositions), with the nickel volume fraction along the x-axis and the forsterite to forsterite plus silicate melt ratio (noted as Fo/(Fo+Melt)) along the y-axis. This figure indicates different states of textural maturation as a function of these two parameters. The most texturally equilibrated textures are obtained for low Fo/(Fo+Melt) ratios. At a fixed Fo/(Fo+Melt) ratio, increasing the metal volume fraction causes the metallic blobs to be more and more irregular, except for a ratio of 70% where variations in the metal content do not seem to affect the shape of the blobs anymore. These features highlight that for the same micro-textural equilibrium (dihedral angles), different macro-textural properties can be achieved.

Figure 4: Textural evolution of nickel phase in PC samples with varying Fo/(Fo+Melt) (90% in red, 80% in blue and 70% in green) and varying nickel content (10 vol% in the first column, 15 vol% in the second one and 20 vol% in the third one). The textural differences observed on Figure 3 are quantified using the Normalized Surface (NS) as a function of blob volume (a-c) and the volume fraction distribution (d-f). The NS populations are compared with equivalent aspect ratios predicted for simple geometrical shapes to have an indication of how much the blobs deviate from a reference shape. In this aim, ticks on the right y- axis (a, b, c) represent the wire equivalent aspect ratio (height to diameter). At a given nickel fraction, the general trend of the NS population is affected by the Fo/(Fo+Melt) ratio with low ratios fostering the presence of rounded grains (NS values close to 1). The bin to bin nickel volume fraction distributions (d-f) show the same effect for the Fo/(Fo+Melt) ratio. The presence of small localized networks that can reach up to 10 vol% of the total nickel is also highlighted, a feature likely to arise from the cold compression that forces the nickel to form a network. These localized networks represent remnants of a larger network that broke apart. Each single NS population at each temperature step is plotted in Figure S2.

Figure 5: 3D view of the five largest nickel blobs at different temperature steps of the <65 : 25 : 10> PE experiment (1-6) and at the peak temperature for the <70 : 5 : 25> (7) and <65 : 5 : 30> (8) PE experiments. Each inset corresponds to one data point on Figure 6. The largest blobs seems to form a network from the beginning of the experiment in the <65 : 25 : 10> mixture (1-3), but the four other largest blobs still have a significant size. However, these blobs constantly evolve as their location constantly changes at each temperature step, with a dynamic of local interconnections and disruptions. Once a given temperature has been reached (slightly above

the silicate solidus and nickel liquidus), the large network breaks apart into smaller blobs which become more and more rounded with increasing temperature and time (4-6), indicating that the initial state was not a stable configuration. For PE experiments with larger Ni contents (7 and 8), the largest blob constitutes a much widespread network and does not evolve with time, arguing in favor of persistent networks. As these 3D networks have irregular shapes, it may be difficult to see any details; for a comparison between the 3D views and the 2D slices on each face of the cube, the reader is referred to Figure S4.

Figure 6: Evolution of textural properties of nickel phase in the PE experiments conducted at beamline PSICHE (SOLEIL Synchrotron) for three different mixtures: <65 : 25 : 10> (in red), <70 : 5 : 25> (in green) and <65 : 5 : 30> (in blue). Results are plotted as a function of temperature, which corresponds also to a different silicate melt content due to progressive melting. For simplicity, the nickel volume fraction (a) and the NS (b) of the largest blob are plotted as a function of temperature. 3D views of each numbered data point are represented on Figure 5. In the <65 : 25 : 10> sample, right after compression, nickel is forced to form a network that represents about 60-70 vol% of the total nickel (1-3), due to different rheological properties between the metal and silicates. However, this metal content is much lower than the expected interconnection threshold, and increasing temperature and silicate melt content cause the network to be disrupted into smaller blobs (3-6) with shapes more and more rounded (i.e. NS approaching 1). In opposition to that, networks formed in the experiments containing 25 and 30 vol% keep the exact same characteristics during the whole time of experiment: their largest blob clusters more than 99 vol% of the total nickel and have NS with constant values. These networks are thus persistent and above the interconnection threshold. Hence, the interconnection threshold of nickel in a partially molten silicate matrix lies between 20 and 25 vol%.

Figure 7: NS (a-c) and volume fraction (d-f) distribution of all detected blobs in the PE experiments as a function of temperature (color code). The <65 : 25 : 10> shows once more the presence of a forced network from the beginning of the experiment. However upon network disruption, blobs quickly rearrange to form spheres, with a decrease of the NS toward a value of 1 and an increase of the proportion of blobs in the range 10^3 to 10^5 μm^3. At the end of experiment, volume fraction distributions are almost identical to the most texturally evolved PC samples (Figure 4). Samples hosting larger silicate melt contents (25 and 30 vol%) show NS populations and volume fraction distributions that do not evolve during the time of experiment, arguing strongly in favor of a persistent network and of an interconnection threshold of pure nickel in partially molten silicate matrix between 20 and 25 vol%. Each single NS population at each temperature step is plotted in Figure S3.

Figure 8: (a.) Evolution of the normalized total surface area of nickel blobs during the <65 : 25 : 10> PE experiment. Grey dots represent the data extracted from the 3D data while the color lines represent the evolution of the normalized total surface area of forsterite grains calculated from grain growth law (see equation (3)) along the followed temperature path (black line). Both metallic blob and forsterite grain surfaces area are normalized by their initial values. The parameters of the growth laws for our experimental system (olivine + silicate melt + nickel) are taken from Guignard et al. (2016 and 2012) and Guignard (2011) for solid and partially molten conditions, respectively, while those for Fe-FeS melt – olivine systems representative of literature studies are taken from Solferino et al. (2015) and Solferino and Golabek (2018). This figure indicates that the textural maturation

of nickel grains is limited by grain growth of the rigid silicate matrix. Although the forsterite powder was sieved, data are best fitted within a range of initial grain sizes between 10 and 20 µm, indicating that cold compression crushed the forsterite grains. (b.) Evolution of the normalized total surface area for our PC experiments (black curve) and the studies of Yoshino et al. (2003), Roberts et al. (2007) and Watson and Roberts (2011), and Bagdassarov et al. (2009) respectively in green, blue and red. Our experiments were conducted with a partially molten silicate subsystem and modeled using grain growth laws of Guignard (2011) while that in the literature were performed below the silicate solidus and modeled with grain growth laws of Guignard et al. (2016 and 2012). The thick full lines show the evolution that occurred during the time of experiment, while the thin dashed lines indicate the further evolution that would have occurred for longer times. Such plot shows that our experimental conditions and those of (Bagdassarov et al., 2009) allow a slight decrease of the normalized total surface area which may not allow the evolution to fully equilibrated textures but ensures that any forced interconnected network can break apart. On the contrary, experimental conditions of Yoshino et al., (2003), Roberts et al., (2007) and Watson and Roberts (2011) do not allow any evolution of the normalized total surface area during the time of experiment, artificially making the initially forced interconnected network persistent over the experiment. It is of note that thermal histories of planetesimals have timescales on the order of ten million years, which would ensure the disruption of any forced network.

Figure 9: Textures of iron-rich phases in a suite of natural objects that experienced increasing peak: (a.) Forest Vale H4 ($T_{peak} \approx 800$ K) chondrite, (b.) Misshof H5 ($T_{peak} \approx 1100$ K) chondrite, (c.) Estacado H6 ($T_{peak} \approx 1200$ K) chondrite (H4, H5 and H6 pictures from Guignard and Toplis, 2015), (d.) Acapulco ($T_{peak} \approx 1373$ K, Acapulco -2 from MNHN), (e.) chondrule of Yamato 81020 ($T_{peak} \approx 1773$ - 1873 K, picture from Ganino et al. (2019) used with permission of authors). Troilite grains appear in orange while kamacite-taenite grains appear in white; the gray matrix corresponds to the silicates.

Figure 10: Degree of non-circularity ΔC (in %) of the iron-rich phases in the suite of natural objects shown in Figure 9: Forest Vale H4, Misshof H5, Estacado H6, Acapulco and Lodran, and chondrules of Yamato 81020, respectively in black, dark gray, light gray, red and green. These distributions indicate that the degree of non-circularity decreases with increasing peak temperature. However, sections of Acapulco and Lodran ($\Delta C \approx 35\%$) have intermediate textures between H4 ($\Delta C \approx 50\%$) and H5 ($\Delta C \approx 20\%$) chondrites, while based on their peak temperature, they would have been expected to have textures intermediate between H6 ($\Delta C \approx 10\%$) chondrites and chondrules ($\Delta C \approx$ 2-3%). This anomalous feature indicates that the extraction of a silicate melt and subsequent compaction of the parent body, forced the textures of iron-rich phases to be irregular. Once silicate grains grow up to a few hundred microns, as in primitive achondrites, the extraction of the silicate melt freezes grain sizes and the irregular textures, as growth processes are drastically hindered.

Declaration of competing interests

 The authors declare that they have no known competing financial interests or personal relationships that could have appeared to influence the work reported in this paper.

☐The authors declare the following financial interests/personal relationships which may be considered as potential competing interests:

Credit Author Statement

Adrien Néri: Conceptualization, Methodology, Formal analysis, Investigation, Writing – Original Draft, Writing – Review & Editing, Visualization**, Jérémy Guignard:** Conceptualization, Investigation, Writing – Original Draft, Writing – Review & Editing, Supervision**, Marc Monnereau:** Conceptualization, Investigation, Writing – Original Draft, Writing – Review & Editing, Supervision**, Misha Bystricky:** Conceptualization, Investigation, Writing – Review & Editing**, Jean-Philippe Perrillat:** Investigation, Writing – Review & Editing**, Denis Andrault:** Investigation, Writing – Review & Editing**, Andrew King:** Methodology, Software, Investigation, Writing – Review & Editing**, Nicolas Guignot:** Methodology, Investigation**, Christophe Tenailleau:** Methodology, Investigation**, Benjamin Duployer:** Methodology, Investigation**, Michael J. Toplis:** Conceptualization, Validation, Writing – Review & Editing, Supervision**, Ghylaine Quitté:** Funding acquisition, Conceptualization, Investigation, Writing – Review & Editing, Supervision

Highlights

-3D tomography study of the interconnectivity of nickel in a partially molten silicate

-Forced interconnection at the beginning of the experiment due to cold compression

-The interconnection threshold of nickel in such system lies between 20 and 25 vol%

-Low interconnection thresholds of iron-sulfur melts are questioned due to compression

-Variability of textures in primitive achondrites explained by matrix compaction